Ultralow thermal conduction and impurity scattering in Cu_2HgSnS_4: An Hg-harnessed diamondlike semiconductor for thermoelectric devices

Sumit Kukreti [ORCID], Surbhi Ramawat [ORCID], and Ambesh Dixit [ORCID]*

*Advanced Materials and Device (A-MAD) Laboratory, Department of Physics,
Indian Institute of Technology Jodhpur, Jodhpur, Rajasthan 342030, India*

Among the most sought-after chalcogenides, Hg-based diamondlike semiconductors have recently been realized for ultralow low heat conduction and potential thermoelectric devices. We present a less well-known but promising quaternary Hg-based chalcogenide, Cu_2HgSnS_4 (CHTS), for its electrical and thermal transport properties and compare it to its parent compound Cu_2ZnSnS_4 (CZTS) for better insight. CHTS is observed with distinct Hg-S and other bond pair strengths, but CZTS has similar cation-anion bond strengths, signifying anharmonicity caused by the heavy element Hg. Phonon dispersion in the Hg-dominated top acoustic frequency zone is nearly flat, indicating reduced phonon group velocity. The avoided-crossing characteristic, a sign of coupling in both high-frequency acoustic and lower-frequency optical modes, is also evident in the same region. The Hg atom's weak binding and considerable vibration with avoided crossing resemble cagelike skutterudite rattling. An ultralow glasslike average lattice thermal conductivity (κ_l) of $\sim 0.53\,\mathrm{W\,m^{-1}\,K^{-1}}$ at 300 K is noticed and associated with overall lower phonon group velocity, mild anharmonicity, and a lower avoided-crossing frequency. At higher temperatures, κ_l decreases to $0.23\,\mathrm{W\,m^{-1}\,K^{-1}}$ at 573 K, comparable to typical Hg-based tellurides such as $Cu_2HgGeTe_4$ and $Cu_2HgSnTe_4$ ($\kappa_l < 0.25\,\mathrm{W\,m^{-1}\,K^{-1}}$) and noticeably smaller than the κ_l of known $Cu_2HgSnSe_4$ nanoparticles. A large power factor for *p*-type doped structures is ascribed to an increased Seebeck coefficient because of the high-density-of-state effective mass close to the valence-band edge. The isoelectronic environment of CZTS and CHTS band edges should make them conduct similarly. This is further confirmed while comparing the estimated electrical conductivity of CHTS with the experimental data of CZTS for moderate doping concentration. Furthermore, in modest concentrations, holes with Ionized impurity scattering as their principal limiter have lifetimes of ~ 10 fs. A *p*-type Figure of Merit (ZT) value >2.0 is obtained with moderate doping of $\sim 10^{18}$ to $10^{19}\,\mathrm{cm^{-3}}$ at 700 K. These remarkable ZT and ultralow lattice thermal conductivity characteristics suggest CHTS's promise for intermediate-temperature thermoelectricity, making it easier to implement devices using the same material.

I. INTRODUCTION

With the potential for the reversible conversion of heat energy into electrical energy through the Seebeck and Peltier effects, thermoelectric materials have ushered in a new era of innovation to address the global energy demand [1–3]. In thermoelectric devices, the energy conversion efficiency is often determined by the dimensionless figure of merit defined as $zT = \sigma\,S^2\,T\,(\kappa_e + \kappa_l)^{-1}$, where σ is electrical conductivity, S is the Seebeck coefficient, T is absolute temperature, and κ_l and κ_e correspond to lattice and electronic thermal conductivity, respectively. Thus, a low thermal conductivity with a large power factor (PF) $\sigma\,S^2$ is the key for an efficient thermoelectric device. However, the coupling of σ, S, and κ_e makes a big challenge to tune a single parameter in order to achieve higher ZT for a TE material. However, several approaches have been proposed to improve TE performance, including adjusting the carrier concentration for large power factors, band engineering, and introducing defects and dislocations to reduce thermal conductivity via enhanced phonon scattering [4,5]. However, materials with intrinsically low lattice thermal conductivity are in prime focus to realize efficient TE devices.

In the past few decades, diamondlike, multinary-chalcogenide semiconductors have gained recognition for their potential in several key fields, including photovoltaics, optoelectronics, and various energy-related devices. The most well known of them are zinc blende GaAs, ZnSe, chalcopyrite $CuInTe_2$, $CuIn_xGa_{1-x}Se_2$ (CIGS), and related quaternary Cu_2ZnSnS_4 (CZTS), among others [6–10]. Significantly, the diamondlike structure (DLS), which is tetrahedrally linked, gives them stability, tunability, and adaptability for a variety of applications. Nevertheless, the strong covalent bonding in these compounds is considered to possess significant thermal conductivity and, therefore, is understood to preclude thermoelectric applications [11,12]. However, in the last few years, several discoveries have upended this presumption by demonstrating lower κ_l and higher mobility in some DLSs, which hence served as better thermoelectric devices. For instance, some tellurides and mercury-based chalcogenides have been extensively studied and shown to have high

carrier mobilities and low thermal conductivities, which was attributed to the presence of heavy elements Hg and Te as well as the phonon scattering from Cu_{Hg} and Hg_{Cu} antisite defects for optimized doping, but further optimization of carrier concentration is required to enhance the thermoelectric efficiency [13]. Strikingly, strategies like nanostructuring, doping, and varying the chemical composition are well employed in DLSs for ZT enhancement [14–17], such as in $Cu_2CoSnSe_xS_{4-x}$, for which low κ_l and enhanced power factor can approach 0.75 ZT for intermediate temperature [18]. A record ZT value of 1.6 at $\sim$800 K was recently realized in a Na-doped CZTS single crystal with a thermal conductivity of $\sim$0.94 W m^{-1} K^{-1} [19]. In addition, the available literature on various selenide materials (such as $Cu_2FeSnSe_4$, $Cu_2CdSnSe_4$, and $Cu_2ZnGeSe_4$) shows that the quaternary materials have much lower lattice thermal conductivity than their binary and ternary counterparts. However, the chemical complexity of quaternary DLS due to native defects and secondary phases during fabrication makes them sensitive to growth conditions [13,20–22].

Instead, in most thermoelectric materials, it has been observed that the overall ZT becomes constrained when multiple techniques, such as doping and alloying, are employed to achieve lower κ_l. This usually happens because of the inevitable scattering of charge carriers due to the introduction of defects and doping. Therefore, the search for materials with intrinsically low lattice thermal conductivity continues as a first option to realize efficient thermoelectric materials and exhibit reduced complexity in device fabrication. More importantly, the possibility of decoupled electron and phonon transport while using inherently low-κ_l materials always gives an upper hand in independent control over the electronic transport properties, which could simply be achieved by regulating the band structure near the Fermi level.

Furthermore, to understand the possibility of lower lattice thermal conduction, several reports have focused on probing the phonon anharmonicity and looking at its dependence on the electronic, bonding, and orbital configurations [23–27]. The atomic mass is also one of the deciding factors as thermal conductivity is related to the inverse of mean atomic weight via the Keyes expression [28]. Typical examples are diamond having 2200 W m^{-1} K^{-1}, silicon with 156 W m^{-1} K^{-1}, and heavier germanium reported with a minimum of $\sim$60 W m^{-1} K^{-1} [29]. This is often consistent in many chalcopyrites and chalcogenides [30,31]. Some exceptions are also noticed, which do not adhere to the Keyes rule. For example, in comparison to the lighter $CuAlS_2$, chalcopyrite tellurides like $CuAlTe_2$ and $CuAlSe_2$ have a higher thermal conductivity [30]. This anomaly is present in various rare-earth-based binary compounds in addition to chalcopyrite [32–36]. Here, it is asserted that the metavalent character of the cations, which results in considerable lattice distortion, enhances phonon anharmonicity and gives sulfides a lower κ_l than selenides and tellurides [37]. Moreover, additional factors that are supposed to contribute to a low phonon velocity and further suppress the lattice thermal conductivity include the softening of optical modes and the lower value of avoided-crossing frequency resulting from a strong coupling between acoustic and lower optical phonon modes [38–40]. Considering the importance

of DLS and especially Cu-based quaternary chalcogenides Cu_2-II-IV-(S/Se)$_4$ (II = Zn, Cd, Hg; IV = Si, Ge, Sn) having sufficient mobility and the possibility of lower thermal conductivity in heavy-element-based materials, we investigated the thermal properties of Cu_2HgSnS_4 (CHTS), a compound semiconductor. This substance is closely related to Cu_2ZnSnS_4, which has been extensively studied for photovoltaic and thermoelectric applications. The presence of numerous cation ordering motifs in close energetic proximity to one another in quaternary DLS typically causes the stannite phase of CHTS to remain stable while the kesterite phase of CZTS becomes more favorable from an energetic standpoint [13,41,42].

Furthermore, in a study on its selenide counterpart $Cu_2HgSnSe_4$, it is revealed that the localization of the hole conducting bands in the $[Cu_2Se_2]$ slabs preserve hole mobilities from being influenced by the structural complexity of the quaternary crystals, permitting the concurrence of higher mobility with intrinsically low thermal conductivity. The reported $Cu_2HgSnSe_4$ nanoparticles with different material compositions yielded Seebeck coefficients up to $160\,\mu$V K^{-1}, electrical conductivity $\sim$10^4 S m^{-1}, and thermal conductivity down to 0.5 W m^{-1} K^{-1} at intermediate temperature [43]. Additionally, as pointed out in our previous study, metals like CHTS's ductility and its alloy composition also allow flexible devices [44]. This was demonstrated through its estimated Pugh ratio ($\sim$3.2), which is larger than the critical value (1.75) of ductile and brittle boundary [45]. Moreover, since $Cu_2HgGeTe_4$ and $Cu_2HgSnTe_4$ have recently been shown to be promising TE materials, the thermal study of Cu_2HgSnS_4 becomes significant; yet, the thermoelectric properties of CHTS are still largely unexplored.

In this work, we comprehensively analyze the thermoelectric properties of the Cu_2HgSnS_4 and its correlations with bonding character, electronic configuration, and phonon dynamics via first-principles methods, including *ab initio* scattering and transport theory. We begin with structural analysis by quantifying the strength of the chemical bonds of CHTS and comparing it with the parent CZTS, indicating a sign of the Hg-S soft bond nature. Examining the electronic band structure reveals overall dispersive bands near both band edges and the multiple band convergence near the valence-band edge, ultimately benefiting the thermoelectric. Furthermore, using three phonon scattering mechanisms, we tried to understand the phonon transport and realize a signature of anharmonicity indicated by a large-mode Grüneisen parameter contributed by acoustic phonon modes dominated by Hg atoms. Both particlelike and wavelike propagations of phonons are considered to compute total lattice thermal conductivity owing to the ultralow thermal conduction similar to highly anharmonic and glasslike solids. Next, analyzing the lattice and impurity scattering, the carrier relaxation time is computed along with the implication of carrier concentration as well. Herein, we also correlated most of the properties with the well-available Cu_2ZnSnS_4 data for better insight. Consequently, we reveal that Cu_2HgSnS_4 with low thermal conduction $\sim$0.39 W m^{-1} K^{-1} at 500 K could be a potential material at intermediate temperature as ZT reaches $\gtrsim$ 1.0 for *p*-type doping.

II. METHODOLOGY

A. Electronic structure calculation

The density functional theory calculations are performed with the full-potential linearly augmented plane-wave (FP-LAPW) approximation as implemented in WIEN2k [46] and the Vienna Ab initio Simulation Package (VASP) based on the projector augmented wave (PAW) method [47]. The electronic structure is calculated in WIEN2k. The modified Becke-Johnson (TB-mBJ) potential [48] along with Hubbard parameter [$U = 0.52$ Ry (7.705 eV) for Cu $3d$ and Hg $4d$ electrons], and spin-orbit coupling is opted for better approximation in band-gap value. This choice of method along with the U value is borrowed from the available literature where experimental and theoretical studies proposed an appropriate Hubbard parameter for Cu_2HgSnS_4 [49]. The parameters like the plane-wave cutoff $R \times K_{max}$, the wave function inside the sphere expanded up to l_{max}, and G_{max}, the charge density cutoff, are taken 8, 10 and 14 (a.u.)$^{-1}$ respectively, in conjunction with -6 Ry Ecut (the core valence separation energy). The self-consistent field calculations are employed with 1500 k-points, and force and energy tolerances are kept at 0.001 Ry/bohr and 0.0001 Ry.

The electronic scattering rates, lifetime, and mobility are evaluated using the *ab initio* scattering and transport (AMSET) code [50], which solves the linearized electronic Boltzmann transport equation. AMSET has been shown to perform well in estimating transport properties when compared to both experimental observation and other highly accurate theoretical methods using the EPW code [51]. Specifically, scattering-mechanism-dependent transport properties are examined under the consideration of scattering from acoustic deformation potential (ADP), ionized impurities (IMP), and polar optical phonons (POPs). In ADP and IMP scatterings, electrons do not acquire or lose energy, showing elastic scattering, while POP is an inelastic scattering because it occurs due to phonon emission or absorption. Here the elastic scattering rate is calculated using the momentum relaxation time approximation while the self-energy relaxation time approximation is utilized for computing the inelastic scattering rate. The Fermi golden rule is used to calculate the scattering rates for elastic and inelastic scatterings from an initial nk state to a final $mk + q$ state and can be written as Eqs. (2) and (3) [50]:

$$\tau^{-1}_{nk \to mk+q} = \frac{2\Pi}{\hbar} |g_{nm}(\boldsymbol{k}, \boldsymbol{q})|^2 \delta(\varepsilon_{nk} - \varepsilon_{mk+q}), \quad (2)$$

$$\tau^{-1}_{nk \to mk+q} = \frac{2\Pi}{\hbar} |g_{nm}(\boldsymbol{k}, \boldsymbol{q})|^2 \left[(n_q + 1 - f^0_{mk+q}) \right.$$
$$\times \delta(\Delta\varepsilon^{nm}_{k,q} - \hbar\omega_q) + (n_q + f^0_{mk+q})$$
$$\left. \times \delta(\Delta\varepsilon^{nm}_{k,q} + \hbar\omega_q) \right], \quad (3)$$

where $\hbar$, δ, n, and f are the Planck's constant, Dirac delta function, Bose-Einstein distribution, and Fermi-Dirac distribution. The ε_{nk} corresponds to the energy of the $|nk\rangle$ state and $g_{nm}(\boldsymbol{k}, \boldsymbol{q})$ is the electron-phonon coupling matrix element of the considered scattering mechanism. The $-\hbar\omega_q$ and $+\hbar\omega_q$

correspond to the photon emission and absorption. Instead of using the constant relaxation time approach, AMSET estimates relaxation time using a different band and k-point-dependent scattering approaches. The total scattering (τ^{-1}) rate or carrier relaxation time (τ) is estimated by Matthiessen's rule:

$$\frac{1}{\tau} = \frac{1}{\tau^{ADP}} + \frac{1}{\tau^{IMP}} + \frac{1}{\tau^{POP}}, \quad (4)$$

where τ^{ADP}, τ^{IMP}, and τ^{POP} are the relaxation times for ADP, IMP, and POP scattering, respectively. The required parameters to obtain the scattering rates, such as dense and uniform band structures, elastic coefficients, wave-function coefficients, deformation potentials, static and high-frequency dielectric constants, and polar-phonon frequency, are calculated using density functional theory (DFT) and density functional perturbation theory, and details are provided in the Supplemental Material [52]. A convergence test is performed with multiple interpolation factors for best results (see Fig. S4) in the Supplemental Material [52]. Finally, an interpolation factor of 900 is used with the $105 \times 105 \times 55$ dense k grid for converging carrier relaxation time and mobility. Furthermore, using the electronic structure calculations as initially discussed, the Seebeck coefficient, electrical conductivity, and electronic thermal conductivity were calculated by the BOLTZTRAP2 code [53] with reliable carrier relaxation time obtained from the AMSET code.

B. Lattice thermal conductivity and anharmonicity

The chemical bond analysis based on the crystal orbital Hamilton population (COHP) is investigated using the LOBSTER code [54]. The phonon dispersion is obtained using harmonic second-order force constants (IFCs) in PHONOPY [55] through the finite displacement method on a $3 \times 3 \times 1$ supercell, with and without spin-orbit coupling (SOC) taken into consideration (see Fig. S2(a) [52]). The anharmonic third-order IFCs are extracted via the thirdorder.py script of ShengBTE [56], using the real-space supercell approach combined with the DFT calculation implemented by VASP. Here, we employed the $3 \times 3 \times 1$ supercell size with converged interaction cutoff as the eighth-nearest neighbors for fitting to obtain third-order IFCs. The Perdew-Burke-Ernzerhof (PBE) functional of the generalized gradient approximation (GGA) is employed along with a 500 eV kinetic energy cutoff and a $3 \times 3 \times 2$ k-point mesh. Using unified treatment of phonon transport including the contribution of particlelike propagation ($k_p^{\alpha\beta}$) and wavelike tunneling and loss of coherence between different vibrational modes ($k_c^{\alpha\beta}$), the total lattice thermal conductivity ($k_l^{\alpha\beta} = k_p^{\alpha\beta} + k_c^{\alpha\beta}$) is computed using the Wigner formalism. Consider the phonon mode indexed by wave vector $\boldsymbol{q}$ and branch s. The particlelike contribution resulting from the diagonal ($s = s'$) terms of the Wigner heat-flux operator [57] is written as

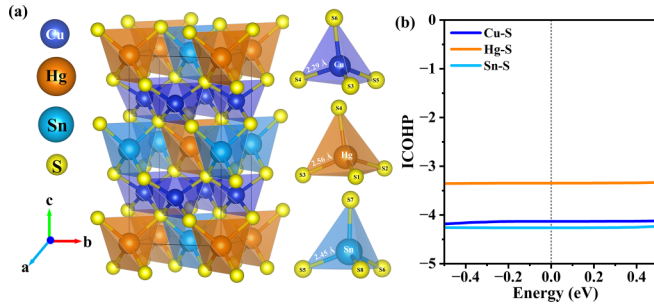$$k_p^{\alpha\beta} = \frac{1}{VN_q} \sum_{\boldsymbol{q}s} C_q^s v_{q,\alpha}^s v_{q,\beta}^s \tau_q^s. \quad (5)$$

FIG. 1. (a) The crystal structure of Cu_2HgSnS_4: the blue, orange, and cyan tetrahedral geometries belong to $[CuS_4]$, $[HgS_4]$, and $[SnS_4]$, respectively. (b) The ICOHPs of the Cu-S, Hg-S and Sn-S bonds near the Fermi level.

The heat carried through the coupling of vibrational modes, described by off-diagonal ($s \neq s'$) terms, is

$$k_c^{\alpha\beta} = \frac{\hbar^2}{k_B T^2 V N_q} \sum_{qs} \sum_{s \neq s'} \frac{\omega_q^s + \omega_q^{s'}}{2} v_{q,\alpha}^{s,s'} v_{q,\beta}^{s,s'}$$

$$\times \frac{\omega_q^s n_q^s (n_q^s + 1) + \omega_q^{s'} n_q^{s'} (n_q^{s'} + 1)}{4(\omega_q^s - \omega_q^{s'})^2 + (\Gamma_q^s + \Gamma_q^{s'})^2} \times (\Gamma_q^s + \Gamma_q^{s'}), \quad (6)$$

where α and β are indexing the Cartesian direction. k_B, V, and N_q are the Boltzmann constant, the volume of the unit cell, and the number of sampled phonon wave vectors in the Brillouin zone, respectively. C_q^s, v_q^s, τ_q^s, ω_q^s, $v_q^{s,s'}$ and Γ_q^s ($\tau_q^s = \frac{1}{\Gamma_q^s}$) are the heat capacity, group velocity, lifetime, phonon frequency, velocity operator, and scattering rate of a phonon mode, respectively. $n_q^s = [\exp(\frac{\hbar \omega_q^s}{k_B T}) - 1]^{-1}$ is the equilibrium Bose-Einstein distribution. The underlying wave mechanism described by the "coherences" term κ_c is phonon interband tunneling between any two propagating modes s and s' with the same q. When the frequencies of the two modes, ω_q^s and $\omega_q^{s'}$, are closer, the wave coherence [$\sim c/(\omega_q^s - \omega_q^{s'})$, where c is the speed of sound] increases, resulting in stronger tunnelling [58].

The phono3py package is employed for computing $k_l^{\alpha\beta}$ [59] using the single-mode relaxation time approximation (SMA) because for ultralow-thermal-conductivity materials the precise Peierls-Boltzmann thermal conductivity is known to be practically indistinguishable from the SMA value [57–60]. In addition, for preparing phono3py input, third-order IFCs are converted to hdf5 format using hiphive [61]. A converged mesh sampling of a $22 \times 22 \times 11$ grid is adopted for thermal conductivity calculation. The mesh and nearest-neighbor convergence test details are provided in Fig. S3 of the Supplemental Material [52].

III. RESULTS AND DISCUSSION

A. Structural and electronic properties

Crystallization of Cu_2HgSnS_4 occurs in the stannite tetragonal phase ($I\bar{4}2m$ space group), as previously reported (Fig. 1). The lattice parameters are borrowed from our previous study and are $a = b = 5.57$ Å and $c = 10.89$ Å, agreeing well with experiments [62]. We see that in Cu_2HgSnS_4, the

Cu, Hg, and Sn atoms are tetrahedrally coordinated by the S atoms with uniform bond lengths of 2.29, 2.56, and 2.45 Å, respectively, and their arrangement follows an edge-sharing pattern. Despite the substitution of Hg^{2+} for Zn^{2+} in the lattice, this structure is nevertheless very close to that of the stannite phase Cu_2ZnSnS_4, except for somewhat higher lattice parameters. However, it is anticipated that substituting Zn with a heavy Hg atom could cause changes in the bond strengths of some cation-anion combinations, perhaps leading to anharmonicity in the system. Considering the possible impact of heavy atoms on the bonding properties, we calculated the COHP and its integration (ICOHP) near the Fermi energy for Cu_2HgSnS_4. This allowed us to measure the bond strength within the unit cell. It is clearly seen that in Fig. 1(b), the |ICOHP| for the Hg-S bond is ~ 3.35, that for the Cu-S bond is ~ 4.15, while for the Sn-S bond it is ~ 4.25. A noticeable difference in |ICOHP| values between Hg-S and other cation-anion pairs represents the relatively soft Hg-S bond and indicates the presence of mild anharmonicity in the system. In addition, the ICOHP for Cu_2ZnSnS_4 was also displayed in Fig. S1 [52], so that we could examine the anharmonicity introduced by the Hg atom upon the substitution of Zn in the parent compound. We see something interesting: the |ICOHP| for Cu-S, Sn-S, and Zn-S all remain between 4 and 4.2, indicating that there is no bond heterogeneity in Cu_2ZnSnS_4 because all cation-ion bonds have same strength, whereas for CHTS all pair strengths differ significantly. Therefore, we can see that the substitution of the heavy element Hg alone can produce a considerable variation in bond strength and is able to generate a small anharmonicity. We can expect that the emerging anharmonicity could contribute to lower heat conduction in Cu_2HgSnS_4 since phonon velocity v_g is proportional to $\sqrt{k/M}$, where k and M stand for bond stiffness and atomic mass, respectively [63]. Thus, we may anticipate that the growing anharmonicity (reflected in terms k and M) may help reduce heat conduction in Cu_2HgSnS_4.

Accurate information of band gap and electronic states near the band edges is essential to predict the material's thermoelectric performance. In Fig. 2, the band structure is shown and is colored according to the fractional amplitudes of the orbitals, which largely contribute near the band edges, i.e., Cu d, Hg d, Sn s, and S p orbitals. It exhibits a direct band gap of ~ 1.33 eV as both conduction-band minimum (CBM) and valence-band maximum (VBM) are located at the Γ point. Noticeably, three bands are found to converge on the Γ point, giving a signature of significant electrical conductivity with the Seebeck coefficient [64,65]. These bands primarily arise due to the hybridization of Cu d and S p orbitals. The Hg d orbital has also made some contributions to these states but mostly determines the deep energy levels inside the valence band; thus, Hg orbitals would be negligibly contributing to the electrical conductivity. As a result, the possibility of altering electrical conductivity in comparison to the Cu_2ZnSnS_4 would also be small because both compounds still have an isoelectronic environment close to their band edges. Additionally, as shown in -COHP in Fig. 2(e), the hybridized orbitals of Cu d and S p strongly contribute as antibonding states below the valence bands. However, the Hg-S bond also appeared to contribute to antibonding states
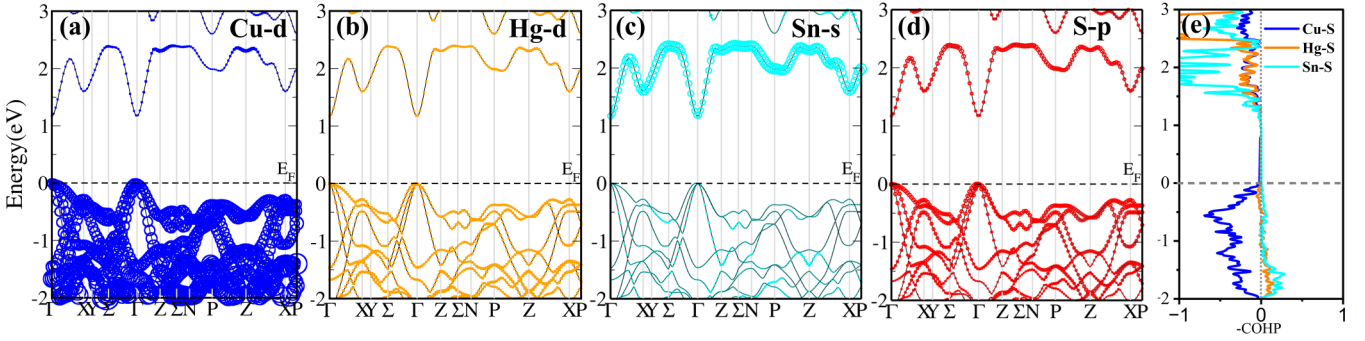
FIG. 2. The orbital projected band structure of Cu_2HgSnS_4 with (a) Cu d, (b) Hg d, (c) Sn s, and (d) S p orbital projection. The diameter of the colored circles is the fractional amplitude of atomic orbitals. (e) The negative COHP of Cu-S, Hg-S, and Sn-S bonds. The states -COHP <0 are showing antibonding while -COHP > 0 represent bonding configuration.

but with little amount. In general, it is anticipated that these antibonding states in the valence bands will reduce the bond strength since they introduce instability with increased system energy [27].

Additionally, there are indications of higher mobility in a highly dispersive conduction band, which is associated with a lower effective mass of electrons compared to holes and would be advantageous for an n-type system (see Table I). Instead, multiple valleys near a few meV above and below the band edges are furthermore anticipated to contribute to the greater power factor as discussed later. According to COHP, Sn s orbitals and S p orbitals close to the conduction-band edge are the main contributors to the strongly dominated Sn-S bond. The overall relatively lower contribution from Hg orbitals, as seen in the projected bands and lower COHP value of the Hg-S bond, further implies the soft bond character of the Hg-S bond, which is also visible through the ICOHP, as mentioned above.

B. Phonon properties

In order to understand the micromechanism of lattice dynamics the phonon dispersions with phonon partial density of states (Ph-DOS) are computed based on PBE+SOC estimated force constants and drawn along the directions Z-Γ-X-P-Γ-N of the Brillouin zone [Fig. 3(a)]. The dynamic stability is confirmed by the absence of imaginary phonon modes. Cu_2HgSnS_4 has an eight-atom primitive cell, so 24 phonon modes are seen for all q points, of which 3 are acoustic and the other 21 are optical. We see a gap between high-frequency and low-frequency optical modes, which often results from the substantial range of atomic masses of constituent elements. Notably, the acoustic modes <1.3 THz [shaded region in Fig. 3(a)] show more or less flat branches along all directions, which may provide the system with significant phonon

scattering or low phonon velocity and, thereby, low lattice thermal conductivity. Additionally, phonon-phonon scattering appears to be aided by the lower optical modes (above ~ 1.3 THz), which also exhibit some smaller dispersion with hybridized areas. Due to a large dispersion in the middle-frequency region ($2 < \omega < 3.75$ THz), it is expected to have a large phonon group velocity, so a significant contribution to the total κ_l.

It is interesting to note that the flat region of acoustic modes lying in lower-frequency regions is where the heavy element Hg contributes most. The avoided crossing between acoustic and optical branches can also be noticed by further magnifying the phonon dispersion near this region [zoomed view in Fig. 3(a)], which manifests the coupling between lower optical and topmost acoustic branches. A little contribution of Cu and Sn is visible in acoustic modes but primarily contributes in the middle-frequency optical modes. In contrast, a higher region of optical modes is dominated by the lighter element S. This is consistent with the commonly known trend of lowering phonon frequency with higher atomic mass. In order to better comprehend how the nature of the vibrations and the crystal structure relate to one another, we computed the amplitude of atomic vibration at the Γ point for the 4th and 24th branches, as shown in Fig. 3(b), while that for the 1st and 12th branches is presented in Fig. S2(b) [52]. The large vibrational amplitude of the Hg atom for the fourth phonon branch [the bottom one of Fig. 3(b)] again confirms its large populated density of states observation in the shaded region of phonon dispersion. The topmost 24th optical branch with largely dominated S-atom vibration with partially observed Sn vibration is also confirms the lightest atom vibration at a higher frequency as per the convention [top one of Fig. 3(b)]. Furthermore, the temperature-dependent mean squared displacements in Fig. S2(c) [52] also signify the higher amplitude of the Hg atom. Overall, the vibrational feature of Hg, like weak bonding and significant vibrational contribution, indicates a kind of atomic rattling that is analogous to the rattling in cagelike compounds such as clathrates and skutterudites where the loosely bound guest atoms rattle in the host cage structures and scatter the heat-carrying phonons [38,66]. Additionally, the localization of phonon modes in the lower as well as higher frequencies may lead to scattering centers which may further assist for lower thermal conduction.

TABLE I. The computed effective masses of electron and hole of Cu_2HgSnS_4 at CBM and VBM (in m_0), where $m_0 = 9.1 \times 10^{-31}$ kg.

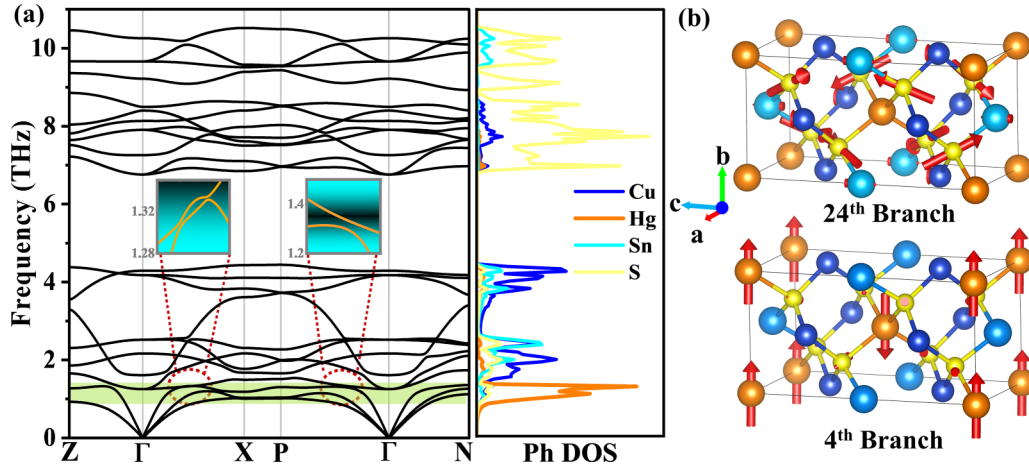| CBM (m_0)			VBM (m_0)		
Γ-X	Γ-Z	Γ-Σ	Γ-X	Γ-Z	Γ-Σ
0.109	0.148	0.148	0.214	0.324	0.324

FIG. 3. (a) Phonon dispersion along Z-Γ-X-P-Γ-N directions and phonon density of states (Ph-DOS) contributed by constituent atoms considering spin-orbit coupling. The light green shaded region highlights the less dispersive band belonging to the acoustic frequency. This region is mainly dominated by Hg atom vibration, as visible in the intense orange color peak in the Ph-DOS. The dotted circle indicates the avoided-crossing area between acoustic and optical modes, which are shown at the magnified view in the inset. (b) Atomic vibration at the Γ point corresponds to the 4th branch (bottom) and 24th branch at top, where the atomic displacement is indicated by red arrows while the orange, blue, cyan, and yellow spheres represent Hg, Cu, Sn, and S atoms, respectively. A significant vibration of Hg is well captured as the 4th branch lies in the shaded region of phonon dispersion.

C. Particlelike contribution to κ_l

Initially the particlelike lattice thermal conductivity (κ_p) for Cu_2HgSnS_4 is calculated. Its temperature variations perpendicular to the *ab* plane or crossplane ($\kappa_p^\perp$) and parallel to the *ab* plane or in plane ($\kappa_p^\parallel$) with their average (κ_p^{avg}) are shown in Fig. 4. With changing temperatures, it is noticed that κ_p^{avg} follows an inverse, i.e., $\sim T^{-1}$, relation, which can be correlated with the conventional phonon gas model and enhancement of the phonon-phonon scattering with an increase in temperature. The computed $\kappa_p^\parallel$ and $\kappa_p^\perp$ values at 300 K are ~ 0.46 and ~ 0.37 W m^{-1} K^{-1}, respectively, as shown in Fig. 4(a). A small anisotropy in κ_p could possibly arise due to uneven phonon transport in these directions. Next, it is crucial to obtain the cumulative κ_p to ascertain the contribution of various phonon frequencies to the total κ_p. For this, we examine the derivative of κ_p with respect to the phonon frequency at 300 and 500 K as shown in Fig. 4(b). Even though the majority of the peaks are in the acoustic range (<1.3 THz), it is noted that the lower optical frequency zone considerably contributes to the overall κ_p. Hence, similar to other Cu-based chalcogenides, the κ_p of Cu_2HgSnS_4 is also non-negligibly impacted by the optical modes, as seen by the normalized κ_p as a function of frequency. For instance, at 300 K, nearly half of the total κ_p is supplied by the lower optical modes from the 1.3 to 4.2 THz region, such as 47% and 45% to $\kappa_p^\parallel$ and $\kappa_p^\perp$, respectively, while the acoustic modes contribute 40% and 50% in both directions. A significant contribution of higher optical modes >6.8 THz, i.e., $\sim 13\%$ and 5% to $\kappa_p^\parallel$ and $\kappa_p^\perp$, is detected for heat carriers. For both temperatures, a similar κ_p distribution is observed over frequency. Overall, it is confirmed that more than half of the total κ_l value originates from the optical frequency region, hence strongly influencing the heat conduction in Cu_2HgSnS_4 material. Moreover, the impact of particle size is examined in Fig. 4(c) by plotting the mean free path (MFP) dependency

of $\kappa_p^\parallel$ and $\kappa_p^\perp$ at temperatures of 300 and 500 K. It is evident that the short MFP (<10 nm) dominates the thermal transport in Cu_2HgSnS_4. For a 50% reduction in the κ_p value, the MFP for $\kappa_p^\parallel$ and $\kappa_p^\perp$ are as short as 1.2 (2.03) nm and 3.27 (5.48) nm at 300 (500) K, respectively, signifying a weak size effect because a significant reduction in κ_p could only be achieved while reducing the size to a very small value or a few nanometers.

Furthermore, to deeply understand the obtained low κ_p, we analyze the frequency-dependent phonon group velocities v_g, Grüneisen parameter γ, and anharmonic scattering rates τ^{-1} [see Figs. 4(d)–4(f)]. According to the kinetic theory, lattice thermal conductivity is given as $\kappa_l = \frac{1}{3}C_v v_g^2 \tau$, where C_v and τ denote specific heat and relaxation time, respectively [63]. We discover a maximum group velocity of 4.28 km s^{-1} near 0.47 THz in the acoustic region. Large v_g values can be seen in the intermediate phonon modes at ~ 2.5 THz as well. These large group velocities can be correlated with the steeper phonon dispersion in these regions and their region of population is consistent when comparing with peaks of the $\frac{d\kappa_p}{d\omega}$ in Fig. 4(b). Instead, due to the moderate phonon dispersion, a smaller group velocity <1.7 km s^{-1} is noticed for higher-frequency modes. While deep monitoring, we also notice a smaller value of v_g near the 1.2 THz region which arises due to the almost flat band geometry and avoided crossing in this acoustic frequency region. Noticeably, the overall v_g in Cu_2HgSnS_4 is still lower than those of moderate-thermal-conductivity materials like the perovskites $SrTiO_3$, $LaWN_3$, etc. [67,68], but are the same order of magnitude as Na_2TlSb, Ba_2AgSb, A_2Se_2, and PbTe with ultralow κ_l [34,69–71]. Furthermore, the computed specific heat appears to be in line with the trend of group velocity, having a larger weightage of lower-frequency but little participation by larger-frequency phonons with the C_V value 8.6×10^{-5} to 6.8×10^{-5} eV, which may serve as a guide for future research [see inset of Fig. 4(d)].
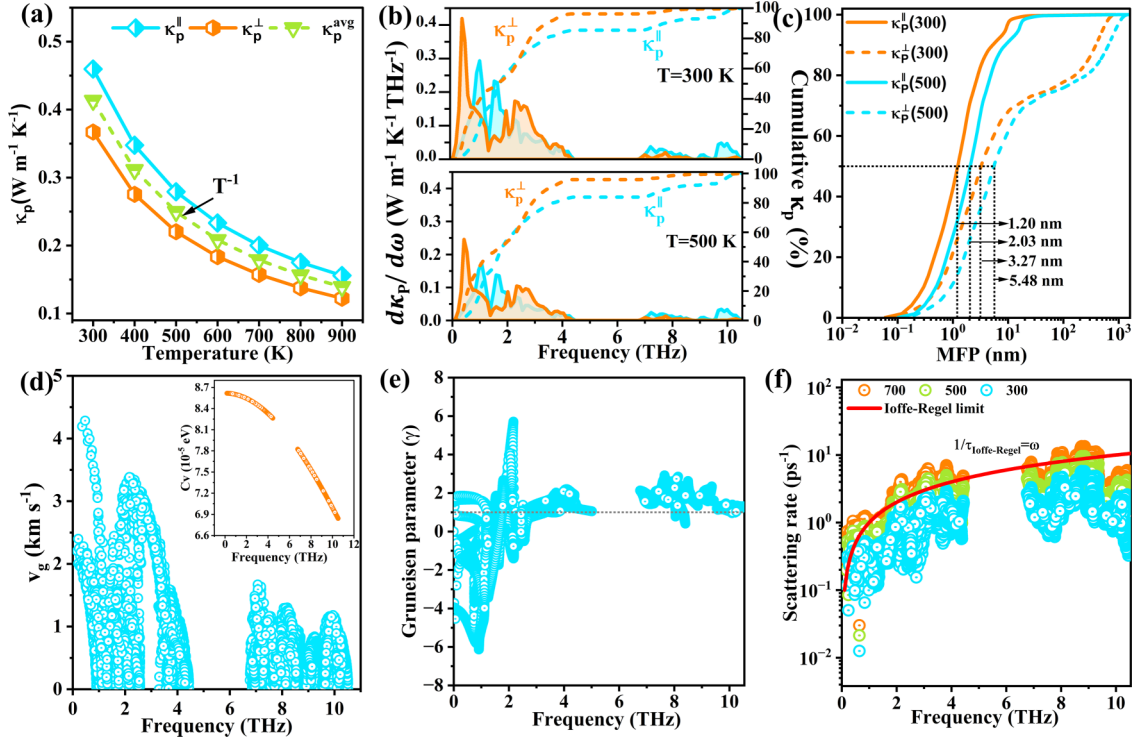
FIG. 4. (a) The calculated particlelike lattice thermal conductivity vs temperature along perpendicular and parallel directions of the *ab* plane. (b) The derivative of κ_l (left scale) with respect to frequency along with the normalized cumulative κ_p (%) vs frequency at 300 K (top) and 500 K (bottom). (c) The calculated normalized cumulative κ_p (%) as a function of the mean free path (MFP) for 300 and 500 K. (d) The frequency-dependent phonon-group velocity. The inset displays specific heat as a function of frequency. (e) The Grüneisen parameter vs frequency with average shown by a dotted line. (f) Anharmonic scattering rate due to three-phonon (3ph) scattering as a function of phonon frequency at 300, 500, and 700 K. The solid red line denotes the Ioffe-Regel limit, defined as $\frac{1}{\tau_{I-R}} = \omega$.

Importantly, the strength of anharmonicity in a periodic crystal is determined by the average Grüneisen parameter (γ). It explains the change in phonon frequency concerning the change in unit-cell volume. Positive or negative values of γ indicate the phonon frequency softening or hardening with the expansion of the lattice [67]. As per the Slack theory, γ is inversely related to the lattice thermal conductivity ($\kappa_l \propto 1/\gamma^2$) [65]. A large negative γ up to the value of -6 for acoustic and lower optical modes <2THz frequency signifies an anharmonicity of phonons in Cu$_2$HgSnS$_4$ and suggests the existence of negative thermal expansion [72]. The average γ value is $\sim$1.0, which is almost comparable to the known thermoelectric materials such as PbSe (1.65) and PbTe (1.69) [62]. Indeed, the heavy element Hg-bonded S atom is the main source of anharmonicity leading to low κ_l, which is also noticed in ICOHP analysis. Moreover, anharmonic scattering rates are another deciding factor for κ_l, which tells us about the possible lifetime of phonons in different frequency regions. In Fig. 4(f), we find a lower value of anharmonic scattering (<1 ps^{-1}) below the 1.3 THz frequency corresponding to the acoustic region. The optical modes mostly appeared to have large scattering rates and signify lower phonon lifetime compared to acoustic modes during heat propagation. Furthermore, to understand the limit of the particlelike contribution of the phonons, the Ioffe-Regel limit $\frac{1}{\tau_{I-R}}$, the limit in which a phonon scattering rate equals its frequency, is drawn over the scattering rate. Phonons whose scattering rate lies

below this reference limit ($\frac{1}{\tau} < \frac{1}{\tau_{I-R}}$) are known to contribute to particlelike thermal conduction while phonons having larger scattering ($\frac{1}{\tau} > \frac{1}{\tau_{I-R}}$) would be crucial to determine the wavelike tunneling similar to amorphous solids and glasses [73,74]. We see that at high temperatures a significant scattering above the Ioffe-Regel limit indicates a non-negligible contribution of wavelike thermal conduction (κ_c) and is therefore considered in the next section.

D. Wavelike contribution to κ_l

The calculated κ_c values for Cu$_2$HgSnS$_4$ along perpendicular and parallel directions are shown in Fig. 5(a). A positive temperature dependence of both $\kappa_c^{\parallel}$ and $\kappa_c^{\perp}$ is noticed as these are found to be $\sim$0.14 (0.17) and $\sim$0.10 (0.12) W m^{-1} K^{-1}, respectively, at 300 (500) K. With the increase in average value (κ_c^{avg}) as $\sim T^{0.28}$ temperature dependence it reaches $\sim$0.16 W m^{-1} K^{-1} at 700 K compared to 0.12 W m^{-1} K^{-1} at room temperature. This signifies the importance of wavelike tunneling of phonons at higher temperatures when κ_p^{avg} reduces with $\sim T^{-1}$ and therefore κ_c become comparable to κ_p. With the added κ_c contribution, the total lattice thermal conductivity at room temperature reaches up to 0.60 and 0.45 W m^{-1} K^{-1} for in-plane and crossplane directions [see Fig. 5(b)] which is almost half of the κ_l of the quartz glass ($\sim$0.9 W m^{-1} K^{-1}). Unlike the T^{-1} trend of κ_p^{avg}, the total average thermal conductivity (κ_l^{avg}) exhibits
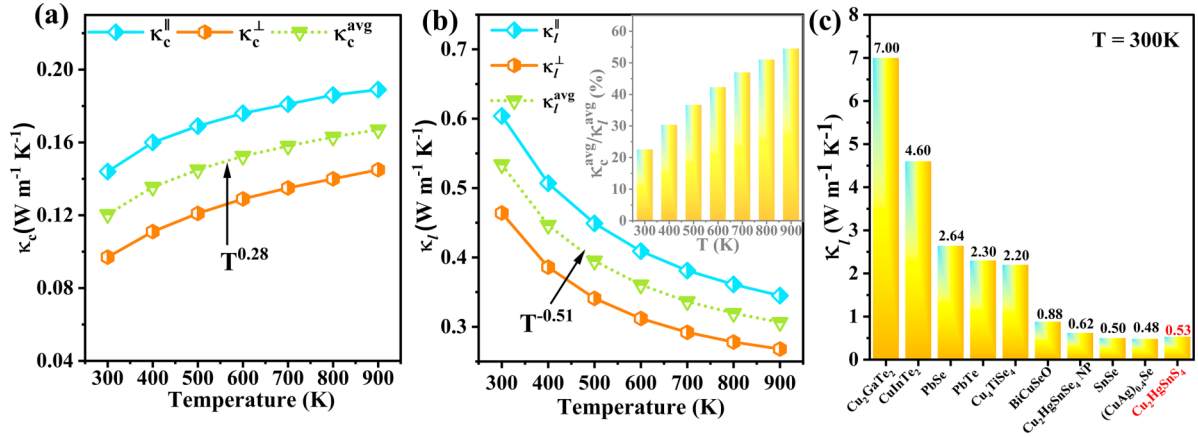
FIG. 5. (a) Calculated wavelike (coherent) lattice thermal conductivity along in-plane ($\kappa_c^{\parallel}$) and crossplane ($\kappa_c^{\perp}$) directions as a function of temperature. The average value (κ_c^{avg}) of both $\kappa_c^{\parallel}$ and $\kappa_c^{\perp}$ is presented by a green dotted line following the increasing function of temperature as $T^{0.28}$. (b) The total lattice thermal conductivity ($\kappa_l = \kappa_p + \kappa_c$) vs temperature variation, in both directions. κ_l^{avg} follows a nonstandard temperature dependence, $\kappa_l^{avg} \propto T^{0.51}$. The inset represents the percentage ratio of wavelike components to total lattice thermal conductivity. (c) A comparison of κ_l for Cu$_2$HgSnS$_4$ with other well-known chalcogenides.

milder decay with temperature, $\sim T^{0.51}$, which is observed in several highly anharmonic crystals. Notably, the $\sim 47\%$ contribution of the wavelike phonon is found for the κ_l^{avg} value, at 700 K, which was $\sim 22\%$ for 300 K as shown in the inset of Fig. 5(b). This evidences the significance of the wavelike contribution to the thermal transport of Cu$_2$HgSnS$_4$ and similar DLS. Strikingly, κ_l^{avg} (~ 0.53 W m^{-1} K^{-1}) is far smaller than for the well-known chalcogenides like PbTe and PbSe, oxides BaTiO$_3$ and PbTiO$_3$, and other DLS-like Cu$_2$CdSnSe$_4$ and Cu$_2$TiSe$_4$ [22,33]. At ~ 573 K (300°), the κ_l^{avg} for Cu$_2$HgSnS$_4$ is ~ 0.37 W m^{-1} K^{-1}, which is even lesser than for Cu$_2$HgSnSe$_4$ nanoparticles [43] and still close to the reported value (< 0.25 W m^{-1} K^{-1}) of Hg-based telluride DLSs such as Cu$_2$HgGeTe$_4$ and Cu$_2$HgSnTe$_4$ at the same temperature [13]. A comparison between the κ_l values of chalcogenides with CHTS is also shown in Fig. 5(c).

Therefore, due to significant scattering of high-frequency phonon modes with lower group velocity, and lower heat capacity, these modes play a key role in limiting the total lattice thermal conduction, whereas relatively lower scattering, in particular one order less of scattering rates corresponding to the lower acoustic frequency with an enhanced v_g, is contributing positively to the total κ_l. Additionally, the wavelike tunneling of phonons is adding a significant contribution to the total thermal transport. Thus, the overall smaller v_g values, anharmonicity due to the heavy Hg atom, and lower avoided-crossing frequency are realized as the joint reason for ultralow lattice thermal conductivity in stannite Cu$_2$HgSnS$_4$.

E. Transport properties

The evaluation of the TE performance in semiconductors also depends on the scattering mechanism of carriers; hence the current work considers three crucial types of carrier scattering: ADP scattering, IMP scattering, and POP scattering. In the literature, we see that IMP and POP scattering do have a more significant effect on electronic transport in terms of carrier lifetime over the generally considered ADP scattering based on deformation theory [75,76]. Therefore, these met-

rics are drawn for both electron (*n*-type) and hole (*p*-type) doping in Fig. 6. While plotting the overall and scattering resolved average lifetime as a function of temperature for a fixed doping concentration 1×10^{19} cm^{-3}, in Figs. 6(a) and 6(c), we observe a decrease in overall lifetime from 2.5×10^{-14} s (1×10^{-14} s) to 1.2×10^{-14} s (8×10^{-15} s) for the electron (hole) while elevating temperature from 300 to 900 K. The ADP and POP lattice scattering-based lifetimes decrease with temperature while IMP remains almost constant as it does not change too much in all temperature ranges. A large IMP scattering is found to be the key factor for reducing the total lifetime value. Through the illustration of scattering events near the band edges [see Figs. 6(b) and 6(e)], it is clearer that in Cu$_2$HgSnS$_4$ the scattering magnitude follows the order IMP > POP > ADP. The complex band geometry accompanying multiple valleys and more dense energy bands facilitates a sophisticated scattering pattern in the vicinity of the valence-band edge. On the other side, very few bands present near the conduction-band edge are providing relatively less dense scattering events. Especially at ~ 1.7 eV energy, another valley from the conduction band appeared to collectively increase all the scattering events.

In addition, by varying the carrier concentration we try to understand its effect on transport. We observe the dominance of POP scattering at lower concentrations or nominally doped regions, say, 10^{17} cm^{-3}, while at large carrier concentration it diminishes, and IMP scattering becomes more prominent, of the order $\sim 10^{14}$ s^{-1} at both band edges, to decide the carrier's lifetime and mobility (see Figs. S5–S7 [52]). Nevertheless, regardless of carrier concentration, ADP scattering is largely inconsequential because it almost remains unchanged except for a small increase in higher concentration and happens at a much slower rate than the other mechanism. This nature may have developed because of acoustic phonon and carrier coupling that was essentially identical at low carrier concentrations and slightly enhanced at higher carrier concentrations. The lower values of deformation potentials (~ 3.9 eV for the valence band and ~ 2.9 for the conduction band) are another factor contributing to the ADP scattering's lack of
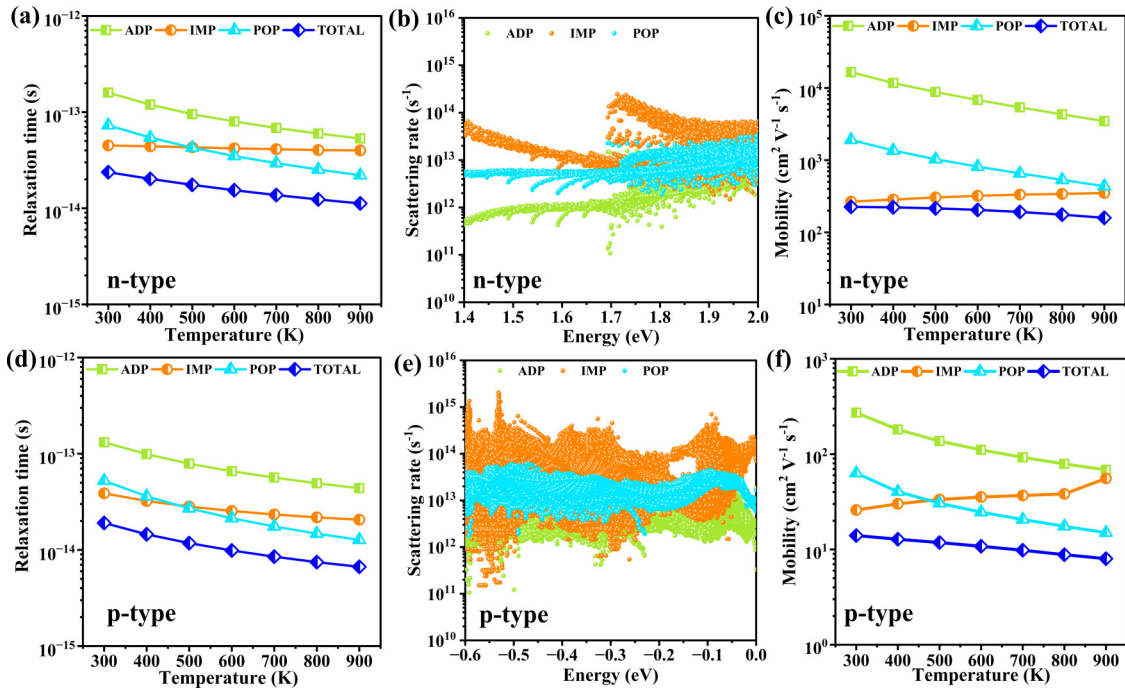
FIG. 6. [(a), (d)] ADP, IMP, and POP scattering-mechanism-based relaxation time as a function of temperature for *n*-type and *p*-type doping, and [(b), (e)] their scattering rate near the conduction- and valence-band edges as a function of energy at 300 K. The dominance order of scattering near the band edges is IMP > POP > ADP. [(c), (f)] The overall and all individual scattering resolved mobilities vs temperature for *n*-type and *p*-type doping. In all the results 1×10^{19} cm^{-3} doping concentration is considered.

significance. The nondominant ADP scattering also aligns with other studies on Cu$_4$TiSe$_4$, BaSnS$_3$, LaAgOS/Se, A$_2$Se$_2$, and CaCuP [71,75,77–79].

Furthermore, the overall carrier mobility values are $\sim$225.0 (14.0) cm^2 V^{-1}s^{-1} and $\sim$159.0 (8.0) cm^2 V^{-1}s^{-1} for the electron (hole) at 300 and 900 K, respectively [see Figs. 6(c) and 6(f)]. ADP, POP, and the overall mobilities follow a decreasing trend with increasing temperature which is attributed to the enhancement in phonon density and respective scattering events at high temperatures. However, it is generally seen that the IMP scatterings remain almost unaffected by temperature; the same is reflected by the consistent contribution of their mobility in the all-temperature range. Overall, the higher mobility of electrons compares to the holes due to the large dispersion in the conduction band and rather complex and less dispersed valence bands indicates the possibility of enhanced electrical conduction while using *n*-type doping.

Furthermore, we determined Seebeck coefficients (S), electrical conductivity, power factor, and electronic thermal conductivity against the carrier concentration (10^{17}–10^{21} cm^{-3}) at 300, 500, and 700 K for *n*-type and *p*-type doping along the in-plane and crossplane direction. This range of doping can be accomplished by commonly used chemical doping techniques, which alter carrier concentrations to regulate chemical potential to imitate the doping process without adding actual dopants to the system [80]. While observing, we found that at $\sim$1 $\times$ 10^{19} cm^{-3} carrier concentration, the value of |S| for the electron (hole) is $\sim$45.4 (245.5) µV K^{-1} at 300 K and $\sim$101.79 (253.4) µV K^{-1} at 700 K along the in-plane direction. In the crossplane direction, |S| is $\sim$45.27 (235.0) µV K^{-1}

for 300 K and $\sim$100.3 (244.8) µV K^{-1} for 700 K [Figs. 7(a) and 7(e)]. Here, the S values are almost isotropic and hence can be thought of as independent of the crystallographic orientation and could also be attributed to the almost equal effective mass along Γ-X and Γ-Z directions. As can be seen, |S| for *p*-type doping is nearly two times that of the *n*-type configuration, and this would be a crucial attribute to aid in the production of high thermoelectricity in Cu$_2$HgSnS$_4$.

Furthermore, the higher Seebeck coefficient is also correlated with the higher density of states effective mass near the band edges as given by $m_d^* = N_v^{2/3} m_b^*$, where N_v denotes the orbital's degeneracy and m_b^* is the average effective mass of degenerate valleys [59,60]. This implies that, for a given carrier concentration, the Seebeck coefficient can be either due to a large degeneracy, N_v, or large m_b^*. In Cu$_2$HgSnS$_4$, due to the complex band geometry of the valence band, both N_v and m_b^* are larger around the valence-band edge compared to the conduction-band edge, facilitating larger m_b^*, and hence serve relatively large Seebeck coefficient value for *p*-type doping. Instead, for both doping configurations, the absolute value of S decreases with the increasing carrier concentration while rising along temperature elevation. This trend is in parallel to the relation $S = \frac{8\pi^2 k_B^2 T}{3eh^2} \times (\frac{\pi}{3n})^{\frac{2}{3}} \times m_d^*$, where n and h show carrier concentration and Planck's constant, respectively [81]. It signifies that the tuning carrier concentration could be an effective strategy to achieve a large S.

Figures 7(b) and 7(f) demonstrate the variation of electrical conductivity σ with carrier concentration. With increasing ρ, σ seems to follow the trend of mobility, i.e., rising constantly. This is because of its direct dependence on carrier mobility as
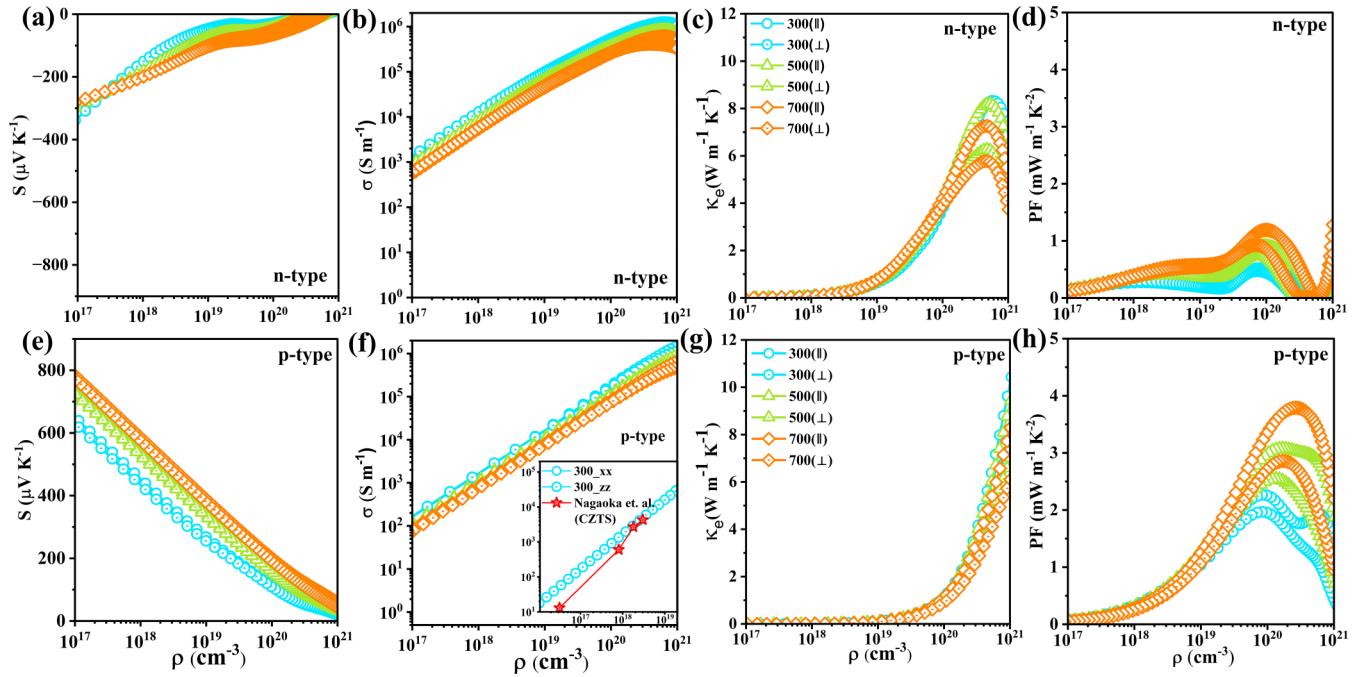
FIG. 7. Electronic transport properties of Cu_2HgSnS_4 as a function of carrier concentration with temperatures 300, 500, and 700 K along in-plane and crossplane directions: [(a), (e)] Seebeck coefficient, [(b), (f)] electrical conductivity, [(c), (g)] electronic thermal conductivity, and [(d), (h)] power factor for *n*-type and *p*-type doping, respectively. Inset of (f) shows a comparison of our estimated σ of CHTS with *p*-type CZTS crystal at 300 K.

$\sigma = ne\mu$, where n, e, and μ are the carrier concentration, unit charge, and charge carrier mobility, respectively. For example, at 300 K and 2.5×10^{18} cm^{-3} doping, along the crossplane direction, σ_e (σ_h) is $\sim 3.0 \times 10^4$ (0.41×10^4)S m^{-1}, while at higher carrier concentrations such as 1×10^{20} cm^{-3}, it increases to $\sim 5.4 \times 10^5$ (1.8×10^5)S m^{-1}. Interestingly, our results on *p*-type doping show good agreement with σ values for moderately doped *p*-type CZTS crystal for the range $\sim 10^{18}$ to $\sim 10^{19}$ cm^{-3}, as shown in the inset of Fig. 7(f). For instance, at 3.0×10^{18} cm^{-3} *p*-type doping, σ is reported to be 0.42×10^4 S m^{-1} for CZTS [19], which is close to 0.41×10^4 S m^{-1} for CHTS at 2.5×10^{18} cm^{-3} doping. These findings seem consistent with our previous analysis that replacing Zn with Hg would not significantly alter the electrical conductivity of CHTS because σ primarily depends on carrier properties near the Fermi level or the band edges. Again, in both CHTS and CZTS, an isoelectronic orbital dominance from Cu and S atoms confirms similar electrical conductivity. Furthermore, at a higher temperature range due to strong carrier phonon coupling, a large scattering results in a lower σ value. This is visible by the decrease in σ, around even one order of magnitude for electrons, and a significant change for the hole as well at the same carrier concentration.

In order to determine the optimal doping for an excellent thermoelectric material, the trend of power factor (PF $= \sigma S^2$) as a function of carrier concentration plays a key role [Figs. 7(d) and 7(h)]. The PF reaches a peak value at the optimal carrier concentration when the increase in σ and the decrease in S achieve a balance. For instance, at 700 K, we see that the PF first increases to near $\sim 1 \times 10^{20}$ cm^{-3} and afterward shows a sharp reduction for

both electron and hole doping. The anisotropic PF arises due to the anisotropy in S and σ along different axes at the same temperature. Further monitoring the *p*-type doping, we noticed that a significant difference in S value serves a maximum PF ~ 2.26 mW m^{-1} K^{-2} at 300 K. At the same time, the peak is at ~ 3.79 for 700 K. Interestingly, this value of PF is sufficiently larger than those for the recently reported CZTS single crystal (1.6 mW m^{-1} K^{-2}) [19], chalcopyrite CuGaTe$_2$ (1.25 mW m^{-1} K^{-2}) [82], and Sb$_{0.1}$Ge$_{0.9}$Te$_{0.88}$Se$_{0.12}$ (~ 2.88 mW m^{-1} K^{-2}) at 700 K [83]. On the other side for *n*-type doping a smaller PF of value 0.52 mW m^{-1} K^{-2} is found at 300 K due to the lesser σ while at higher temperature, ~ 700 K, it touches 1.19 mW m^{-1} K^{-2} just because of the one order of increase in σ.

In Figs. 7(c) and 7(g), the electronic thermal conductivity is plotted, which is one-to-one related with σ via the Wiedemann-Franz law $\kappa_e = L\sigma T$, where L is the Lorenz number, which, however, varies in semiconductors with the doping level [84]. We see κ_e increases with carrier concentration and is slightly affected by temperature. Furthermore, κ_e is found to be nearly insignificant in the low-carrier-concentration regime to the 1×10^{20} cm^{-3} doping region. Above this carrier concentration, κ_e increases for both types of doping and achieves a value comparable to the lattice thermal conductivity κ_l. For example, at $\sim 1 \times 10^{19}$ cm^{-3} and along the in-plane direction, the κ_e remains at 0.65 (0.15) W m^{-1} K^{-1} at 300 K and was found to be ~ 0.77 (0.12) W m^{-1} K^{-1} for the electron (hole) at 700 K. Hence, the maximum total thermal conductivity ($\kappa_e + \kappa_l$, $\kappa_l = 0.38$ W m^{-1} K^{-1}) at 700 K is ~ 0.50 W m^{-1} K^{-1} for *p*-type CHTS, which is still far smaller than that of
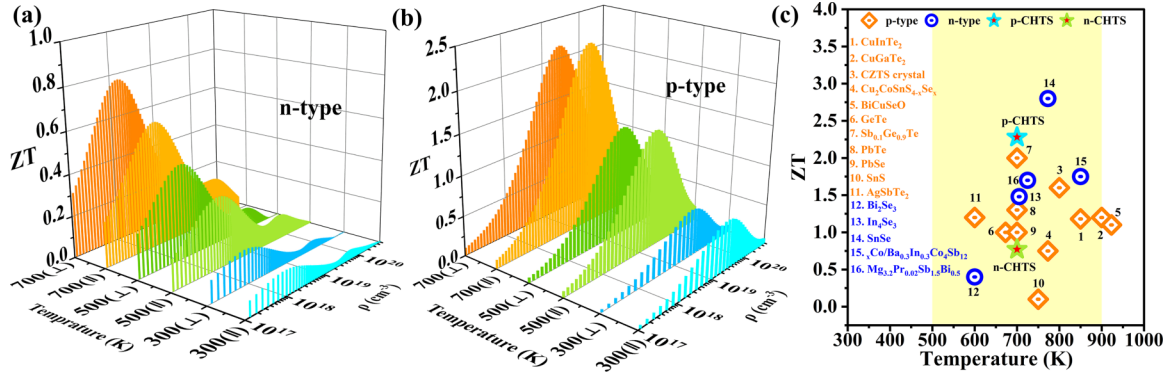
FIG. 8. [(a), (b)] The predicted figure of merit ZT as a function of carrier concentration along in-plane and crossplane directions at 300, 500, and 700 K for n-type and p-type doping, respectively. (c) ZT comparison among well-known p-type and n-type thermoelectric materials with Cu_2HgSnS_4. The rectangular and circular symbols represent the p-type and n-type doped materials, respectively. The stars show our estimated maximum ZT for both types of doping. The yellow shaded region highlights the intermediate-temperature range.

the CZTS crystal (~ 1.23 W m^{-1} K^{-1}) [19]. Overall, the effective power factor for the intermediate-temperature range, even for both n- and p-type carrier concentrations, would provide a better opportunity for efficient thermoelectric application.

F. Figure of merit

Hence, after analyzing all the transport properties comprehensively, we investigated the ZT for the 300–700 K range. In Figs. 8(a) and 8(b), we depicted the computed ZT as a function of carrier concentration for stannite Cu_2HgSnS_4. Generally, most of the quaternary chalcogenides show intrinsically p-type behavior. However, in this analysis, we considered both n-type and p-type possibilities in Cu_2HgSnS_4. It shows nearly similar values in all directions for corresponding carrier concentrations and temperatures with a slight anisotropy. For instance, at 500 K the computed ZT value for n type (p type) doping is ~ 0.45 (1.46), and at higher temperatures, say, 700 K, it reaches the maximum value of ~ 0.77 (2.28) at an optical carrier doping level $\sim 2 \times 10^{18}$ cm^{-3} ($\sim 2 \times 10^{19}$ cm^{-3}) along the crossplane direction. Since the ZT values for p-type doping are approximately three times those of n-type doping, p-type doping could effectively enhance the TE performance of Cu_2HgSnS_4. The difference in n- and p-type ZT could be attributed to the aforementioned variance in Seebeck coefficient (at 500 K, $S_n = 76.26$ µV K^{-1} and $S_p = 328.23$ µV K^{-1}) and, hence, a large power factor for the p-type system is due to the large density of states effective mass near the valence-band edge. Notably, at 700 K, the estimated ZT for p-type CHTS exceeds well from the CZTS crystal (~ 1), chalcopyrite $AgInTe_2$ (~ 2), $CuGaTe_2$ (~ 0.4), etc. [19,82,85]. However, for n-type doping, the ZT remains lower than the n-type SnSe (~ 2.8 at 773 K) [86]. The predicted ZTs for p-type Cu_2HgSnS_4 are also comparable to other DLSs like $Cu_2HgSnTe_4$, $Cu_2CoSnSe_4$, and other commercially available PbTe [see Fig. 8(c)]. Moreover, the obtained optimal doping concentrations are also practically relevant in bulk materials like DLSs. Hence, a significant power factor along with ultralow lattice thermal conductivity makes the Cu_2HgSnS_4 suitable for intermediate-temperature thermoelectric applications.

IV. CONCLUSION

In summary, we systematically analyzed the thermal and electronic transport properties of a quaternary DLS, i.e., stannite Cu_2HgSnS_4, via first-principles calculations combined with Boltzmann transport theory. Unlike Cu_2ZnSnS_4, the heavy atom Hg contributes a modest amount of anharmonicity to the system, as inferred from the ICOHP values. The relatively weak binding of the Hg atom and demonstration of a significant vibration are similar to the rattling mode in cagelike compounds. The noticed avoided crossing between acoustic and low-frequency optical modes also corroborates the same and indicates lower thermal conduction. The noticed significant density of states effective mass near the valence-band edge facilitates a large Seebeck coefficient for p-type systems. Cu and S mainly contribute to the band edges; therefore, the Hg cation in place of Zn does not seem to alter electrical conductivity compared to the known DLS, Cu_2ZnSnS_4. In contrast, the impact on phonon dynamics due to Hg atoms leads to an ultralow value of $\kappa_l \sim 0.53$ W m^{-1} K^{-1} at 300 K, which further drops to ~ 0.39 and ~ 0.33 at 500 and 700 K, respectively. The dominance of IMP scattering decides the overall mobility in Cu_2HgSnS_4 compared to ADP and POP scattering mechanisms. Finally, the maximum ZT values, such as 2.28 for p type and 0.77 for n type at 700 K, are reported in the range of $\sim 10^{19}$ cm^{-3} doping concentration. Our present study on Cu_2HgSnS_4 serves the underlying transport mechanism in Hg-based chalcogenides and introduces it as the most efficient thermoelectric material at intermediate temperatures belonging to the DLS family.

[1] P.-C. Wei, C.-N. Liao, H.-J. Wu, D. Yang, J. He, G. V. Biesold-McGee, S. Liang, W.-T. Yen, X. Tang, J.-W. Yeh, Z. Lin, and J.-H. He, Thermodynamic routes to ultralow thermal conductivity and high thermoelectric performance, Adv. Mater. **32**, 1906457 (2020).

[2] T. M. Tritt and M. A. Subramanian, Thermoelectric materials, phenomena, and applications: A bird's eye view, MRS Bull. **31**, 188 (2006).

[3] J. Mao, H. Zhu, Z. Ding, Z. Liu, G. A. Gamage, G. Chen, and Z. Ren, High thermoelectric cooling performance of n-type Mg_3Bi_2−based materials, Science **365**, 495 (2019).

[4] Q. Yan and M. G. Kanatzidis, High-performance thermo-electrics and challenges for practical devices, Nat. Mater. **21**, 503 (2022).

[5] S. Hao, V. P. Dravid, M. G. Kanatzidis, and C. Wolverton, Computational strategies for design and discovery of nanostructured thermoelectrics, npj Comput. Mater. **5**, 58 (2019).

[6] H. Katagiri, K. Jimbo, W. S. Maw, K. Oishi, M. Yamazaki, H. Araki, and A. Takeuchi, Development of CZTS-based thin film solar cells, Thin Solid Films **517**, 2455 (2009).

[7] S. C. Riha, B. A. Parkinson, and A. L. Prieto, Solution-based synthesis and characterization of Cu_2ZnSnS_4 nanocrystals, J. Am. Chem. Soc. **131**, 12054 (2009).

[8] A. E. Delahoy, L. Chen, M. Akhtar, B. Sang, and S. Guo, New technologies for CIGS photovoltaics, Sol. Energy **77**, 785 (2004).

[9] J. Yoon, S. Jo, I. S. Chun, I. Jung, H.-S. Kim, M. Meitl, E. Menard, X. Li, J. J. Coleman, U. Paik, and J. A. Rogers, GaAs photovoltaics and optoelectronics using releasable multilayer epitaxial assemblies, Nature (London) **465**, 329 (2010).

[10] S.-H. Wei and S. B. Zhang, Defect properties of $CuInSe_2$ and $CuGaSe_2$, J. Phys. Chem. Solids **66**, 1994 (2005).

[11] J. Qu, C. E. Porter, L. C. Gomes, J. M. Adamczyk, M. Y. Toriyama, B. R. Ortiz, E. S. Toberer, and E. Ertekin, Controlling thermoelectric transport via native defects in the diamond-like semiconductors $Cu_2HgGeTe_4$ and Hg_2GeTe_4, J. Mater. Chem. A **9**, 26189 (2021).

[12] D. Shin, B. Saparov, and D. B. Mitzi, Defect engineering in multinary earth-abundant chalcogenide photovoltaic materials, Adv. Energy Mater. **7**, 1602366 (2017).

[13] B. R. Ortiz, W. Peng, L. C. Gomes, P. Gorai, T. Zhu, D. M. Smiadak, G. J. Snyder, V. Stevanović, E. Ertekin, A. Zevalkink, and E. S. Toberer, Ultralow thermal conductivity in diamond-like semiconductors: Selective scattering of phonons from antisite defects, Chem. Mater. **30**, 3395 (2018).

[14] W. Zhao, Z. Liu, Z. Sun, Q. Zhang, P. Wei, X. Mu, H. Zhou, C. Li, S. Ma, D. He *et al.*, Superparamagnetic enhancement of thermoelectric performance, Nature (London) **549**, 247 (2017).

[15] S. Bin, Z. Han, Y. Jiang, H.-L. Zhuang, J. Yu, J. Pei, H. Hu, J.-W. Li, Y. He, Z. B.-P. Zhang, and J. Li, Re-doped p-type thermoelectric SnSe polycrystals with enhanced power factor and high ZT > 2, Adv. Funct. Mater. **33**, 2301971 (2023).

[16] T. Parashchuk, R. Knura, O. Cherniushok, and K. T. Wojciechowski, Ultralow lattice thermal conductivity and improved thermoelectric performance in Cl-doped $Bi_2Te_{3−x}Se_x$ alloys, ACS Appl. Mater. Interfaces **14**, 33567 (2022).

[17] B. Qin, D. Wang, T. Hong, Y. Wang, D. Liu, Z. Wang, X. Gao, Z.-H. Ge, and L.-D. Zhao, High thermoelectric efficiency realized in SnSe crystals via structural modulation, Nat. Commun. **14**, 1366 (2023).

[18] T. Parashchuk, O. Cherniushok, O. Smitiukh, O. Marchuk, and K. T. Wojciechowski, Structure evolution and bonding inhomogeneity toward high thermoelectric performance in $Cu_2CoSnS_{4−x}Se_x$ materials, Chem. Mater. **35**, 4772 (2023).

[19] A. Nagaoka, K. Yoshino, T. Masuda, T. D. Sparks, M. A. Scarpulla, and K. Nishioka, Environmentally friendly thermo-electric sulphide Cu_2ZnSnS_4 single crystals achieving a 1.6 dimensionless figure of merit ZT, J. Mater. Chem. A **9**, 15595 (2021).

[20] W. G. Zeier, Y. Pei, G. Pomrehn, T. Day, N. Heinz, C. P. Heinrich, G. J. Snyder, and W. Tremel, Phonon scattering through a local anisotropic structural disorder in the thermo-electric solid solution $Cu_2Zn_{1−x}Fe_xGeSe_4$, J. Am. Chem. Soc. **135**, 726 (2013).

[21] C. P. Heinrich, T. W. Day, W. G. Zeier, G. J. Snyder, and W. Tremel, Effect of isovalent substitution on the thermoelectric properties of the $Cu_2ZnGeSe_{4−x}S_x$ series of solid solutions, J. Am. Chem. Soc. **136**, 442 (2014).

[22] M.-L. Liu, I.-W. Chen, F.-Q. Huang, and L.-D. Chen, Improved thermoelectric properties of Cu-doped quaternary chalcogenides of $Cu_2CdSnSe_4$, Adv. Mater. **21**, 3808 (2009).

[23] X. L. Shi, J. Zou, and Z. G. Chen, Advanced thermoelectric design: From materials and structures to devices, Chem. Rev. **120**, 7399 (2020).

[24] J. He, Y. Xia, W. Lin, K. Pal, Y. Zhu, M. G. Kanatzidis, and C. Wolverton, Accelerated discovery and design of ultralow lattice thermal conductivity materials using chemical bonding principles, Adv. Funct. Mater. **32**, 2108532 (2022).

[25] S. Ramawat, S. Kukreti, and A. Dixit, $\beta−SrZrS_3$: A superior intermediate temperature thermoelectric through complex band geometry and ultralow lattice thermal conductivity, Phys. Rev. Mater. **7**, 085403 (2023).

[26] X. song, Y. Zhao, J. Ni, S. Meng, and Z. Dai, High thermoelectric performance in $XAgSe_2$ (X = Sc, Y) from strong quartic anharmonicity and multi-valley band structure, J. Mater. Chem. A **11**, 17138 (2023).

[27] J. Zhang, H. Jiang, X. Xia, Y. Gao, and Z. Huang, Antibonding p-d and s-p hybridization induce the optimization of thermal and thermoelectric performance of $MGeTe_3$ (M = In and Sb,), ACS Appl. Energy Mater. **5**, 15566 (2022).

[28] R. W. Keyes, High-temperature thermal conductivity of insulating crystals: Relationship to the melting point, Phys. Rev. **115**, 564 (1959).

[29] S. Adachi, *Earth-Abundant Materials for Solar Cells: Cu_2-II-IV-VI_4 Semiconductors* (John Wiley & Sons, Inc., Chichester, West Sussex, UK, 2015).

[30] M. L. Valeri-Gil and C. Rincón, Thermal conductivity of ternary chalcopyrite compounds, Mater. Lett. **17**, 59 (1993).

[31] W. Nakwaski, Thermal conductivity of binary, ternary, and quaternary III-V compounds, J. Appl. Phys. **64**, 159 (1988).

[32] S. Lee, K. Esfarjani, T. Luo, J. Zhou, Z. Tian, and G. Chen, Resonant bonding leads to low lattice thermal conductivity, Nat. Commun. **5**, 3525 (2014).

[33] J. M. Skelton, S. C. Parker, A. Togo, I. Tanaka, and A. Walsh, Thermal physics of the lead chalcogenides PbS, PbSe, and PbTe from first principles, Phys. Rev. B **89**, 205203 (2014).

[34] S. Ju, T. Shiga, L. Feng, and J. Shiomi, Revisiting PbTe to identify how thermal conductivity is really limited, Phys. Rev. B **97**, 184305 (2018).

[35] C. Li and D. Broido, Phonon thermal transport in transition-metal and rare-earth nitride semiconductors from first principles, Phys. Rev. B **95**, 205203 (2017).

[36] A. Seko, A. Togo, H. Hayashi, K. Tsuda, L. Chaput, and I. Tanaka, Prediction of low-thermal-conductivity compounds with first-principles anharmonic lattice-dynamics calculations and Bayesian optimization, Phys. Rev. Lett. **115**, 205901 (2015).

[37] L. Elalfy, D. Music, and M. Hu, Metavalent bonding induced abnormal phonon transport in diamondlike structures: Beyond conventional theory, Phys. Rev. B **103**, 075203 (2021).

[38] J. He, M. Amsler, Y. Xia, S. Shahab Naghavi, V. I. Hegde, S. Hao, S. Goedecker, V. Ozoliņš, and C. Wolverton, Ultralow thermal conductivity in full Heusler semiconductors, Phys. Rev. Lett. **117**, 046602 (2016).

[39] Q.-Y. Xie, P.-F. Liu, J.-J. Ma, L.-M. Wu, K.-W. Zhang, and B.-T. Wang, Microscopic mechanisms of glasslike lattice thermal conductivity in tetragonal cubic $Cu_{12}Sb_4S_{13}$ tetrahedrites, Phys. Rev. B **108**, 014302 (2023).

[40] K. M. Ciesielski, B. R. Ortiz, L. C. Gomes, V. Meschke, J. Adamczyk, T. L. Braden, D. Kaczorowski, E. Ertekin, and E. S. Toberer, Strong scattering from low-frequency rattling modes results in low thermal conductivity in antimonide clathrate compounds, Chem. Mater. **35**, 2918 (2023).

[41] N. Sarmadian, R. Saniz, B. Partoens, and D. Lamoen, First-principles study of the optoelectronic properties and photovoltaic absorber layer efficiency of Cu-based chalcogenides, J. Appl. Phys. **120**, 85707 (2016).

[42] Y. K. Kabalov, T. L. Evstigneeva, and E. M. Spiridonov, Crystal structure of Cu_2HgSnS_4, a synthetic analogue of the mineral velikite, Crystallogr. Rep. **43**, 16 (1998).

[43] W. Li, M. Ibáñez, R. R. Zamani, N. García-Castelló, S. Gorsse, D. Cadavid, J. D. Prades, J. Arbiol, and A. Cabot, $Cu_2HgSnSe_4$ nanoparticles: Synthesis and thermoelectric properties, CrystEngComm **15**, 8966 (2013).

[44] S. Kukreti, S. Ramawat, and A. Dixit, Selenizing possibilities of Cu_2HgSnS_4−i.e., $Cu_2HgSn(Se_xS_{1-x})_4$ compound semiconductor: Potential candidate for solar photovoltaics and photodetectors, Physica Status Solidi B: Basic Res. **260**, 2200524 (2023).

[45] O. N. Senkov and D. B. Miracle, Generalization of intrinsic ductile-to-brittle criteria by Pugh and Pettifor for materials with a cubic crystal structure, Sci. Rep. **11**, 4531 (2021).

[46] P. Blaha, K. Schwarz, F. Tran, R. Laskowski, G. K. H. Madsen, and L. D. Marks, WIEN2k: An APW+lo program for calculating the properties of solids, J. Chem. Phys. **152**, 074101 (2020).

[47] P. E. Blöchl, Projector augmented-wave method, Phys. Rev. B **50**, 17953 (1994).

[48] F. Tran and P. Blaha, Accurate band gaps of semiconductors and insulators with a semilocal exchange-correlation potential, Phys. Rev. Lett. **102**, 226401 (2009).

[49] T. V. Vu, A. A. Lavrentyev, B. V. Gabrelian, H. D. Tong, V. A. Tkach, O. V. Parasyuk, and O. Y. Khyzhun, A theoretical and experimental study of the valence-band electronic structure and optical constants of quaternary copper mercury tin sulfide, Cu_2HgSnS_4, a potential material for optoelectronics and solar cells, Opt. Mater. **96**, 109296 (2019).

[50] A. M. Ganose, J. Park, A. Faghaninia, R. Woods-Robinson, K. A. Persson, and A. Jain, Efficient calculation of carrier scattering rates from first principles, Nat. Commun. **12**, 2222 (2021).

[51] S. Poncé, E. R. Margine, C. Verdi, and F. Giustino, EPW: Electron–phonon coupling, transport and superconducting properties using maximally localized wannier functions, Comput. Phys. Commun. **209**, 116 (2016).

[52] See Supplemental Material at http://link.aps.org/supplemental/10.1103/PhysRevB.109.205203 for Cu_2ZnSnS_4 ICOHP (integrated crystal orbital Hamilton population), atomic vibrations of phonon modes, convergence test of phonon transport calculations, and AMSET input parameters and results.

[53] G. K. H. Madsen, J. Carrete, and M. J. Verstraete, BoltzTraP2, a program for interpolating band structures and calculating semiclassical transport coefficients, Comput. Phys. Commun. **231**, 140 (2018).

[54] R. Nelson, C. Ertural, J. George, V. L. Deringer, G. Hautier, and R. Dronskowski, LOBSTER: Local orbital projections, atomic charges, and chemical-bonding analysis from projector-augmented-wave-based density-functional theory, J. Comput. Chem. **41**, 1931 (2020).

[55] A. Togo and I. Tanaka, First principles phonon calculations in materials science, Scr. Mater. **108**, 1 (2015).

[56] W. Li, J. Carrete, N. A. Katcho, and N. Mingo, ShengBTE: A solver of the Boltzmann transport equation for phonons, Comput. Phys. Commun. **185**, 1747 (2014).

[57] M. Simoncelli, N. Marzari, and F. Mauri, Unified theory of thermal transport in crystals and glasses, Nat. Phys. **15**, 809 (2019).

[58] Z. Tong, A. Pecchia, C. Yam, T. Dumitrică, and T. Frauenheim, Glass-like transport dominates ultralow lattice thermal conductivity in modular crystalline $Bi_4O_4SeCl_2$, Nano Lett. **23**, 9468 (2023).

[59] A. Togo, L. Chaput, and I. Tanaka, Distributions of phonon lifetimes in Brillouin zones, Phys. Rev. B **91**, 094306 (2015).

[60] A. Jain, Multichannel thermal transport in crystalline Tl_3VSe_4, Phys. Rev. B **102**, 201201(R) (2020).

[61] F. Eriksson, E. Fransson, and P. Erhart, The hiphive package for the extraction of high-order force constants by machine learning, Adv. Theory Simul. **2**, 1800184 (2019).

[62] S. Kukreti, G. K. Gupta, and A. Dixit, Theoretical DFT studies of Cu_2HgSnS_4 absorber material and $Al:ZnO/ZnO/CdS/Cu_2HgSnS_4$/back contact heterojunction solar cell, Sol. Energy **225**, 802 (2021).

[63] T. M. Tritt, *Thermal Conductivity: Theory, Properties, and Applications* (Springer Science & Business Media, 2005).

[64] Y. Pei, X. Shi, A. Lalonde, H. Wang, L. Chen, and G. J. Snyder, Convergence of electronic bands for high performance bulk thermoelectrics, Nature (London) **473**, 66 (2011).

[65] S. Zulkifal, Z. Wang, X. Zhang, S. Siddique, Y. Yu, C. Wang, Y. Gong, S. Li, D. Li, Y. Zhang, P. Wang, and G. Tang, Multiple valence bands convergence and localized lattice engineering lead to superhigh thermoelectric figure of merit in MnTe, Adv. Sci. **10**, 2206342 (2023).

[66] T. Tadano, Y. Gohda, and S. Tsuneyuki, Impact of rattlers on thermal conductivity of a thermoelectric clathrate: A first-principles study, Phys. Rev. Lett. **114**, 095501 (2015).

[67] Q. Ren, Y. Li, Y. Lun, G. Tang, and J. Hong, First-principles study of the lattice thermal conductivity of the nitride perovskite $LaWN_3$, Phys. Rev. B **107**, 125206 (2023).

[68] M. Tachibana, T. Kolodiazhnyi, and E. Takayama-Muromachi, Thermal conductivity of perovskite ferroelectrics, Appl. Phys. Lett. **93**, 092902 (2008).

[69] T. Yue, Y. Zhao, J. Ni, S. Meng, and Z. Dai, Strong quartic anharmonicity, ultralow thermal conductivity, high band degeneracy and good thermoelectric performance in Na$_2$TlSb, npj Comput. Mater. **9**, 17 (2023).

[70] S.-F. Wang, Z.-G. Zhang, B.-T. Wang, J.-R. Zhang, and F.-W. Wang, Intrinsic ultralow lattice thermal conductivity in the full-Heusler compound Ba$_2$AgSb, Phys. Rev. Appl. **17**, 034023 (2022).

[71] T. Yue, Y. Sun, Y. Zhao, S. Meng, and Z. Dai, Thermoelectric performance in the binary semiconductor compound A_2Se$_2$ (A = K, Rb) with host-guest structure, Phys. Rev. B **105**, 054305 (2022).

[72] V. Gava, A. L. Martinotto, and C. A. Perottoni, First-principles mode Gruneisen parameters and negative thermal expansion in A $-$ ZrW$_2$O$_8$, Phys. Rev. Lett. **109**, 195503 (2012).

[73] E. Di Lucente, M. Simoncelli, and N. Marzari, Crossover from Boltzmann to Wigner thermal transport in thermoelectric skutterudites, Phys. Rev. Res. **5**, 033125 (2023).

[74] P. B. Allen and J. L. Feldman, Thermal conductivity of disordered harmonic solids, Phys. Rev. B **48**, 12581 (1993).

[75] Z. Li, H. Xie, Y. Xia, S. Hao, K. Pal, M. G. Kanatzidis, C. Wolverton, and X. Tang, Weak-bonding elements lead to high thermoelectric performance in BaSnS$_3$ and SrSnS$_3$: A first-principles study, Chem. Mater. **34**, 1289 (2022).

[76] J.-H. Pöhls, S. Chanakian, J. Park, A. M. Ganose, A. Dunn, N. Friesen, A. Bhattacharya, B. Hogan, S. Bux, A. Jain, A. Mar, and A. Zevalkink, Experimental validation of high thermoelectric performance in RECuZnP$_2$ predicted by high-throughput DFT calculations, Mater. Horiz. **8**, 209 (2021).

[77] X.-K. Chen, E.-M. Zhang, D. Wu, and K.-Q. Chen, Strain-induced medium-temperature thermoelectric performance of Cu$_4$TiSe$_4$: The role of four-phonon scattering, Phys. Rev. Appl. **19**, 044052 (2023).

[78] S. Bai, J. Zhang, M. Wu, D. Luo, D. Wan, X. Li, and S. Tang, Theoretical prediction of thermoelectric performance for layered LaAgOX (X = S, Se) materials in consideration of the four-phonon and multiple carrier scattering processes, Small Methods **7**, 2201368 (2023).

[79] J. Willis, I. Bravić, R. R. Schnepf, K. N. Heinselman, B. Monserrat, T. Unold, A. Zakutayev, D. O. Scanlon, and A. Crovetto, Prediction and realisation of high mobility and degenerate p-type conductivity in CaCuP thin films, Chem. Sci. **13**, 5872 (2022).

[80] S.-J. Wang, M. Panhans, I. Lashkov, H. Kleemann, F. Caglieris, D. Becker-Koch, J. Vahland, E. Guo, S. Huang, Y. Krupskaya, Y. Vaynzof, B. Büchner, F. Ortmann, and K. Leo, Highly efficient modulation doping: A path toward superior organic thermoelectric devices, Sci. Adv. **8**, eabl9264 (2022).

[81] J.-C. Lim, S. Y. Kim, W. H. Shin, S. Kim, J. W. Roh, H. Yang, and H.-S. Kim, Characterization of Hall factor with Seebeck coefficient measurement, ACS Appl. Energy Mater. **5**, 4036 (2022).

[82] Y. Cao, X. Su, F. Meng, T. P. Bailey, J. Zhao, H. Xie, J. He, C. Uher, and X. Tang, Origin of the distinct thermoelectric transport properties of chalcopyrite ABTe$_2$ (A = Cu, Ag; B = Ga, In), Adv. Funct. Mater. **30**, 2005861 (2020).

[83] G. C. Shearer, S. Chavan, S. Bordiga, S. Svelle, U. Olsbye, and K. P. Lillerud, Defect engineering: Tuning the porosity and composition of the metal–organic framework UiO-66 via modulated synthesis, Chem. Mater. **28**, 3749 (2016).

[84] M. Jonson and G. D. Mahan, Mott's formula for the thermopower and the Wiedemann-Franz law, Phys. Rev. B **21**, 4223 (1980).

[85] J. J. Plata, E. J. Blancas, A. M. Márquez, V. Posligua, J. Fdez Sanz, and R. Grau-Crespo, Harnessing the unusually strong improvement of thermoelectric performance of AgInTe$_2$ with nanostructuring, J. Mater. Chem. A **11**, 16734 (2023).

[86] C. Chang, M. Wu, D. He, Y. Pei, C.-F. Wu, X. Wu, H. Yu, F. Zhu, K. Wang, Y. Chen, L. Huang, J.-F. Li, J. He, and L.-D. Zhao, 3D charge and 2D phonon transports leading to high out-of-plane ZT in n-type SnSe crystals, Science **360**, 778 (2018).